NORMAL AND OBLIQUE SHOCK-VORTEX INTERACTION

O. Thomer, W. Schröder, E. Krause
Aerodynamisches Institut, RWTH Aachen, Germany
e-mail: oliver@aia.rwth-aachen.de

Breakdown of a slender vortex caused by normal and oblique shocks is studied using numerical solutions of the Euler and Navier-Stokes equations for unsteady, three-dimensional, supersonic flow at free stream Mach numbers of 1.6 and 2.0. At the inflow boundary a Burgers vortex with a given circulation and axial velocity distribution is prescribed. The calculations using approximately 2 million grid points show that breakdown is primarily controlled by pressure forces and is therefore easily initiated when the vortex interacts with a normal shock. Oblique shocks are deformed into an 'S'-shaped part near the vortex core where the shock becomes normal. The results also indicate that initiation of breakdown is more sensitive to variations in the axial velocity than in the circulation, and that the flow structure is clearly time-dependent.

Symbols

a	velocity of sound	x, y, z	cartesian coordinates	superscripts:	
$c_{p,v}$	specific heats	β	dissipative energy flux	^{K}	convective
e	specific total energy	$\delta_{\alpha\beta}$	Kronecker–Delta	^{P}	pressure
$\vec{E},\vec{F},\vec{G}$	fluxes in the x, y and z direction	ϵ	specific internal energy	*	non-scaled variable
J	Jacobian determinant	λ	heat transfer coefficient	subscripts:	
r	core radius	μ	dynamic viscosity	$_a$	advective part
p	pressure	ν	kinematic viscosity	$_d$	diffusive part
$\vec{Q}$	solution vector	ρ	density	$_o$	stagnation conditions
q_β	heat flux vector	τ_{ij}	Stokes stress	$_\infty$	free stream
R	gas constant	Ma	Mach number	$_{+/-}$	left- or right extrapolation
RHS	residual	Pr	Prandtl number		
t	time	Re	Reynolds number		
T	temperature	Sr	Strouhal number		
u, v, w	cartesian velocities	γ	ratio of specific heats (=1.4 air)		
U, V, W	contravariant velocities	ξ, η, ζ	transformed coordinates		

1. Introduction

Recent investigations of flows in turbine engine cascades seem to indicate that shock induced vortex breakdown may be responsible for stall observed at high compressor loads [13]. Although not verified, this conjecture may lead to a new insight and understanding of the stall mechanism. Until now reliable breakdown conditions could not be formulated neither for incompressible nor for compressible flow. Previous investigations mainly dealt with vortices in incompressible flow [1]. For supersonic flow one of the first attempts to derive a breakdown criterion for shock-vortex interaction can be found in [4]. Related to this problem is the leading edge vortex breakdown on delta wings, which was studied numerically by Kandil et al. in [5, 6].

A combined experimental and numerical investigation was initiated at the Aerodynamisches Institut to study shock-vortex interaction. Free stream Mach number, strength of the normal and oblique shocks, and the circulation of the free vortex embedded in the flow were varied in the investigation. Since previously obtained results indicate that breakdown is mainly dominated by pressure forces, it was decided to base the investigation on a numerical solution of the Euler and Navier–Stokes equations for unsteady, three-dimensional, supersonic flow in order to determine the influence of the Stokes stresses and the Fourier heat flux. The study was first purposely restricted to laminar flow, but is presently being extended to turbulent flow by using time-averaged Navier-Stokes equations with several higher order closure assumptions for the Reynolds stresses and the turbulent heat flux.

The breakdown is initiated by letting either an oblique or a normal shock at free stream Mach numbers ranging from 1.6 to 2.0 intersect a slender vortex. In the experiments the strength of the oblique shock is varied

by changing the angle of the shock generating wedge. The circulation of the vortex is varied by changing the angle of attack of a plate of finite span causing the vortex. In the present paper we focus on the discussion of the numerical results and use the preliminary experimental findings to confirm the numerical data qualitatively since no quantitative measurements are available yet.

2. Governing Equations

We numerically solve the NAVIER-STOKES equations for time-dependent three-dimensional, compressible flow. In dimensionless transformed coordinates ξ, η and ζ they read

$$\frac{\partial \hat{Q}}{\partial t} + \frac{\partial \hat{E}_a}{\partial \xi} + \frac{\partial \hat{F}_a}{\partial \eta} + \frac{\partial \hat{G}_a}{\partial \zeta} = \frac{1}{\mathrm{Re}_0}\left(\frac{\partial \hat{E}_d}{\partial \xi} + \frac{\partial \hat{F}_d}{\partial \eta} + \frac{\partial \hat{G}_d}{\partial \zeta}\right) \quad . \tag{1}$$

The REYNOLDS number $\mathrm{Re}_0 = (\rho_0^* a_0^* r_0^*)/\mu_0^*$ is based on stagnation conditions and $\vec{Q}$ is the solution vector, whose components are the the density ρ, the momentum fluxes $\rho\vec{v}$ and the specific energy ρe, multiplied by the Jacobian determinant

$$\begin{aligned} J &= x_\xi y_\eta z_\zeta + y_\xi z_\eta x_\zeta + z_\xi x_\eta y_\zeta - x_\xi y_\zeta z_\eta - y_\xi z_\zeta x_\eta - z_\xi x_\zeta y_\eta = \\ &= (\xi_x \eta_y \zeta_z + \xi_y \eta_z \zeta_x + \xi_z \eta_x \zeta_y - \xi_x \eta_z \zeta_y - \xi_y \eta_x \zeta_z - \xi_z \eta_y \zeta_x)^{-1} \end{aligned} \tag{2}$$

that represents the cell volume, $\hat{Q} = J\vec{Q}$. The fluxes in the ξ, η and ζ directions are

$$\hat{E}_a = J\begin{pmatrix} \rho U \\ \rho U u + \xi_x p \\ \rho U v + \xi_y p \\ \rho U w + \xi_z p \\ U(\rho e + p) \end{pmatrix} \quad \hat{F}_a = J\begin{pmatrix} \rho V \\ \rho V u + \eta_x p \\ \rho V v + \eta_y p \\ \rho V w + \eta_z p \\ V(\rho e + p) \end{pmatrix} \quad \hat{G}_a = J\begin{pmatrix} \rho W \\ \rho W u + \zeta_x p \\ \rho W v + \zeta_x p \\ \rho W w + \zeta_x p \\ W(\rho e + p) \end{pmatrix} \tag{3}$$

$$\hat{E}_d = J\begin{pmatrix} 0 \\ \xi_x \tau_{xx} + \xi_y \tau_{yx} + \xi_z \tau_{zx} \\ \xi_x \tau_{xy} + \xi_y \tau_{yy} + \xi_z \tau_{zy} \\ \xi_x \tau_{xz} + \xi_y \tau_{yz} + \xi_z \tau_{zz} \\ \xi_x \beta_x + \xi_y \beta_y + \xi_z \beta_z \end{pmatrix} \quad \hat{F}_d = J\begin{pmatrix} 0 \\ \eta_x \tau_{xx} + \eta_y \tau_{yx} + \eta_z \tau_{zx} \\ \eta_x \tau_{xy} + \eta_y \tau_{yy} + \eta_z \tau_{zy} \\ \eta_x \tau_{xz} + \eta_y \tau_{yz} + \eta_z \tau_{zz} \\ \eta_x \beta_x + \eta_y \beta_y + \eta_z \beta_z \end{pmatrix} \quad \hat{G}_d = J\begin{pmatrix} 0 \\ \zeta_x \tau_{xx} + \zeta_y \tau_{yx} + \zeta_z \tau_{zx} \\ \zeta_x \tau_{xy} + \zeta_y \tau_{yy} + \zeta_z \tau_{zy} \\ \zeta_x \tau_{xz} + \zeta_y \tau_{yz} + \zeta_z \tau_{zz} \\ \zeta_x \beta_x + \zeta_y \beta_y + \zeta_z \beta_z \end{pmatrix} . \tag{4}$$

In the terms on the right-hand side of equation (1) the abbreviation

$$\beta_j = u_i \tau_{ij} + q_j \tag{5}$$

is used, where

$$\tau_{ij} = \mu\left[\left(\frac{\partial u_i}{\partial x_j} + \frac{\partial u_j}{\partial x_i}\right) - \frac{2}{3}\delta_{ij}\frac{\partial u_k}{\partial x_k}\right] \tag{6}$$

are the STOKES stresses and

$$q_j = -\frac{\mu}{(\gamma-1)Pr}\left(\xi_j \frac{\partial T}{\partial \xi} + \eta_j \frac{\partial T}{\partial \eta} + \zeta_j \frac{\partial T}{\partial \zeta}\right) \tag{7}$$

is the FOURIER heat transfer.

3. Boundary Conditions

The inflow conditions are assumed to be described by a BURGERS vortex centered at x=y=0 together with a radial distribution of the axial velocity component (Fig. 1, plane 5). In dimensionless form the inflow conditions read for constant stagnation enthalpy

$$v_\varphi(r) = \frac{\Gamma_0 \cdot r}{2\pi} \cdot e^{\frac{1-r^2}{2}} \quad ; \quad v_r(r) = 0 \quad ; \quad v_z(r) = v_{z_\infty} \cdot (1 - \delta \cdot e^{-\mu_w \cdot r^2}) \tag{8}$$

$$T(r) = \left[T_\infty - \frac{(\gamma-1)\cdot\Gamma_0^2}{8\pi^2} \cdot e^{(1-r^2)}\right]^1 \quad ; \quad \rho(r) = \left[T_\infty - \frac{(\gamma-1)\Gamma_0^2}{8\pi^2} \cdot e^{(1-\bar{r}^2)}\right]^{\frac{1}{\gamma-1}} \tag{9}$$

$$p(r) = \frac{1}{\gamma} \cdot \left[T_\infty - \frac{(\gamma-1)\Gamma_0^2}{8\pi^2} \cdot e^{(1-\bar{r}^2)}\right]^{\frac{\gamma}{\gamma-1}} = \frac{p^*(r^*)}{\rho_0^* \cdot a_0^*} = \frac{1}{\gamma} \cdot T^{\frac{\gamma}{\gamma-1}}. \tag{10}$$

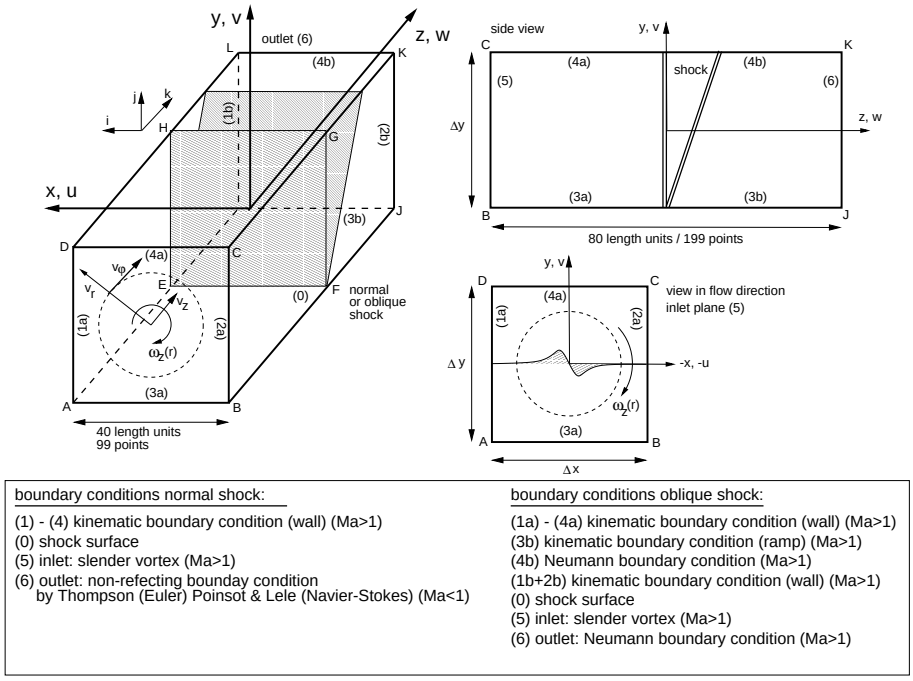

Fig. 1. Computational domain and boundary conditions (left) for normal shock-vortex interaction, breakdown map (center), and flow schematic at time step $t = 200$ (right). Flow is in the positive z-direction.

In the above equations $\Gamma_0 = \Gamma_0^*/(a_0^* r_0^*)$ is the circulation nondimensionalized by the speed of sound at stagnation conditions and the core radius, and $T_\infty = T_\infty^*/T_0^*$ is the free stream temperature nondimensionalized by the stagnation temperature. The azimuthal velocity component v_φ reaches its maximum at $r = 1$, and decreases exponentially with increasing radius $-1 > r > 1$. The circulation at $r^* = r_0^*$ is defined as $\Gamma_0^* = 2 \cdot \pi \cdot r_0^* \cdot v_\varphi^*(r_0^*)$. Because of the exponential decrease of the azimuthal velocity component in the radial direction, disturbances near the axis of the vortex are barely propagated to the lateral boundaries of the computational domain.

For vortices with finite core size the core diameter d is usually defined as twice the radial distance r between the location of the maximum of the azimuthal velocity v_φ and the axis. If the ratio of the diameter d over the length of the vortex l is much smaller than unity, the vortex is called slender implying that the axial velocity $v_z(r)$ is much larger than the radial velocity component $v_r(r)$, i.e.,

$$v_{r\max}/v_\infty = O(d/l) << 1. \tag{11}$$

The slenderness condition also implies that the core radius r_0 is small in comparison to the bursting length l_b, defined as the distance between the inflow cross-section and the breakdown point, i.e., the point where the flow stagnates thereby initiating the breakdown [10].

Controlled via the sign of the parameter $\delta \in [0..1]$ the axial velocity component in the inflow plane is modeled as a 'jet-like' or a 'wake-like' profile, and its radial distribution is given by a GAUSSian distribution. The quantity $r_i = \pm\sqrt{1/(2\mu_w)}$ describes the position of the inflection point of the bell shaped velocity profile. The ratio between the azimuthal and the axial velocity components is defined as the helix angle τ

$$\tau = \frac{v_\varphi^*(r^* = r_0^*)}{v_z^*(r^* = r_0^*)} = \frac{\Gamma_0 \cdot \sqrt{1 + \frac{\gamma-1}{2} Ma_\infty^2}}{2 \cdot \pi \cdot Ma_\infty \cdot (1 - \delta \cdot e^{-\mu_w})} \quad . \tag{12}$$

The above equation shows that τ increases if either the circulation Γ_0 and the wake parameter δ are increased or the MACH number Ma_∞ and the width of the profile μ_w are decreased. The inflow conditions are also used as initial conditions for the entire flow field. The embedded shock in its initial position is given at x=y=0 as a function of the wedge angle α and the shock angle σ by the RANKINE–HUGONIOT relations.

The outflow conditions must be adjusted to the form of the conservation equations used. For the solution of the EULER equations at supersonic outflow, as is the case when an oblique shock interacting with a vortex is considered a simple gradient condition can be applied since all characteristics exit the computational domain.

For subsonic outflow different approximations must be used. Assuming that the axial flow near the outflow cross-section does not experience back flow, TAYLOR series expansions can be used for the EULER and NAVIER-STOKES equations to determine the properties on the boundary via an analytic extension. If it is assumed, that the flow near the outflow cross-section is dominated by a wave mechanism, then at the boundary, waves are propagating out of the computational domain while others are propagating into it. The outgoing waves are described by the solution of the governing equations inside the domain while the inward propagating waves depend on the solution outside of it since vorticity is transported out of the domain of integration. Special care has to be taken in formulating approximate outflow conditions. In the case of subsonic outflow, especially for a time-dependent solution, a simple extrapolation does not seem to describe the local flow situation properly and appears to be arbitrary.

Downstream of the normal shock the flow is subsonic and the characteristics of the governing equations of a viscous fluid become complex. This is the case for steady flow, since then the viscous equations are elliptic, and disturbances from the downstream boundaries can travel upstream into the computational domain, and under certain circumstances could initialize breakdown.

To reduce the reflection of numerical waves at the outflow boundary as much as possible non-reflecting boundary conditions for inviscid flows, as proposed by THOMPSON [15, 16], and for viscous flows, as described by POINSOT ET AL. [11], are imposed in the present investigation. These conditions are based on the LAGRANGEian form of the EULER equations that read in the ξ-direction

$$\begin{aligned}
\left[\frac{\partial p}{\partial t} - \frac{\rho a}{|\nabla\xi|}\left(\xi_x\frac{\partial u}{\partial t} + \xi_y\frac{\partial v}{\partial t} + \xi_z\frac{\partial w}{\partial t}\right)\right] &+ \mathcal{L}_1 = 0 \\
\left[\frac{\xi_x}{|\nabla\xi|}\left(a^2\frac{\partial \rho}{\partial t} - \frac{\partial p}{\partial t}\right) + \frac{\rho a}{|\nabla\xi|}\left(\xi_z\frac{\partial v}{\partial t} - \xi_y\frac{\partial w}{\partial t}\right)\right] &+ \mathcal{L}_2 = 0 \\
\left[\frac{\xi_y}{|\nabla\xi|}\left(a^2\frac{\partial \rho}{\partial t} - \frac{\partial p}{\partial t}\right) + \frac{\rho a}{|\nabla\xi|}\left(-\xi_z\frac{\partial u}{\partial t} + \xi_x\frac{\partial w}{\partial t}\right)\right] &+ \mathcal{L}_3 = 0 \\
\left[\frac{\xi_z}{|\nabla\xi|}\left(a^2\frac{\partial \rho}{\partial t} - \frac{\partial p}{\partial t}\right) + \frac{\rho a}{|\nabla\xi|}\left(\xi_y\frac{\partial u}{\partial t} - \xi_x\frac{\partial v}{\partial t}\right)\right] &+ \mathcal{L}_4 = 0 \\
\left[\frac{\partial p}{\partial t} + \frac{\rho a}{|\nabla\xi|}\left(\xi_x\frac{\partial u}{\partial t} + \xi_y\frac{\partial v}{\partial t} + \xi_z\frac{\partial w}{\partial t}\right)\right] &+ \mathcal{L}_5 = 0 \quad .
\end{aligned} \tag{13}$$

The spatial derivatives of the primitive variables ρ, u, v, w, and p are represented by the wave terms $\mathcal{L}_i$

$$\begin{aligned}
\mathcal{L}_1 &= \lambda_1\left(\frac{\partial p}{\partial x} - \rho a\frac{\partial u}{\partial x}\right) \\
\mathcal{L}_2 &= \lambda_2\left(a^2\frac{\partial \rho}{\partial x} - \frac{\partial p}{\partial x}\right) \\
\mathcal{L}_3 &= \lambda_3\left(\rho a\frac{\partial w}{\partial x}\right) \\
\mathcal{L}_4 &= \lambda_4\left(-\rho a\frac{\partial v}{\partial x}\right) \\
\mathcal{L}_5 &= \lambda_5\left(\frac{\partial p}{\partial x} + \rho a\frac{\partial u}{\partial x}\right) \quad .
\end{aligned} \tag{14}$$

The terms $\lambda_{1,2,3,4,5}$=$u - a$, $u + a$, u, u, u are the eigenvalues of the JACOBIAN matrix in the ξ-direction. A physical interpretation of the eigenvalues can be given by the linearized NAVIER–STOKES equations. According to this approximation the velocities λ_1 and λ_5 represent the convection of pressure waves, λ_2 is the convection velocity of entropy waves, whereas λ_3 and λ_4 are advection velocities of the contravariant velocities along the coordinate lines.

From the above equations (14) the *LODI*–Relations(**L***ocal* **O***ne*–**D***imensional* **I***nviscid*) can be determined

$$\left.\frac{\partial p}{\partial t}\right|_\xi = -\frac{1}{2}(\mathcal{L}_1+\mathcal{L}_5) \tag{15}$$

$$\left.\frac{\partial \rho}{\partial t}\right|_\xi = -\left(\mathcal{L}_2\frac{\xi_x}{|\nabla\xi|}+\mathcal{L}_3\frac{\xi_y}{|\nabla\xi|}+\mathcal{L}_4\frac{\xi_z}{|\nabla\xi|}+\frac{1}{2}(\mathcal{L}_1+\mathcal{L}_5)\right)\frac{1}{a^2} \tag{16}$$

$$\left.\frac{\partial u}{\partial t}\right|_\xi = -\left(\frac{\xi_x}{2\rho a|\nabla\xi|}(\mathcal{L}_5-\mathcal{L}_1)+\frac{1}{\rho a|\nabla\xi|}(\xi_y\mathcal{L}_4-\xi_z\mathcal{L}_3)\right) \tag{17}$$

$$\left.\frac{\partial v}{\partial t}\right|_\xi = -\left(\frac{\xi_y}{2\rho a|\nabla\xi|}(\mathcal{L}_5-\mathcal{L}_1)+\frac{1}{\rho a|\nabla\xi|}(\xi_z\mathcal{L}_2-\xi_x\mathcal{L}_4)\right) \tag{18}$$

$$\left.\frac{\partial w}{\partial t}\right|_\xi = -\left(\frac{\xi_z}{2\rho a|\nabla\xi|}(\mathcal{L}_5-\mathcal{L}_1)+\frac{1}{\rho a|\nabla\xi|}(\xi_x\mathcal{L}_3-\xi_y\mathcal{L}_2)\right) \tag{19}$$

$$\left.\frac{\partial T}{\partial t}\right|_\xi = -\frac{T}{\rho a^2}\left(-\mathcal{L}_2\frac{\xi_x}{|\nabla\xi|}-\mathcal{L}_3\frac{\xi_y}{|\nabla\xi|}-\mathcal{L}_4\frac{\xi_z}{|\nabla\xi|}+\frac{1}{2}(\gamma-1)(\mathcal{L}_1+\mathcal{L}_5)\right) \quad . \tag{20}$$

As long as the flow can be considered as locally one-dimensional and the pressure forces are small the time-dependent change of the primitive variables on the boundary can be determined using the wave amplitudes $\mathcal{L}_i$.

The expansion to three-dimensional, viscous heat conducting flows can be done as follows. The EULER fluxes normal to the outflow boundary are calculated ζ using the characteristic approach described above, and the tangential EULER fluxes, the viscous terms and the heat transfer are calculated using the original governing equations. The assumption of locally one-dimensional flow is still valid. The conservative variables at the outflow boundary can then be written as follows

$$\frac{\partial \rho}{\partial t} = \left.\frac{\partial \rho}{\partial t}\right|_\xi - \eta_x\frac{\partial \rho u}{\partial \eta} - \eta_y\frac{\partial \rho v}{\partial \eta} - \eta_z\frac{\partial \rho w}{\partial \eta} - \zeta_x\frac{\partial \rho u}{\partial \zeta} - \zeta_y\frac{\partial \rho v}{\partial \zeta} - \zeta_z\frac{\partial \rho w}{\partial \zeta} \tag{21}$$

$$\begin{aligned}\frac{\partial \rho u}{\partial t} &= u\left.\frac{\partial \rho}{\partial t}\right|_\xi + \rho\left.\frac{\partial u}{\partial t}\right|_\xi - \eta_x\frac{\partial \rho uu+p}{\partial \eta} - \eta_y\frac{\partial \rho vu}{\partial \eta} - \eta_z\frac{\partial \rho wu}{\partial \eta} - \zeta_x\frac{\partial \rho uu+p}{\partial \zeta} - \zeta_y\frac{\partial \rho vu}{\partial \zeta} - \zeta_z\frac{\partial \rho wu}{\partial \zeta} + \\ &+ \xi_x\frac{\partial \tau_{xx}}{\partial \xi} + \xi_y\frac{\partial \tau_{yx}}{\partial \xi} + \xi_z\frac{\partial \tau_{zx}}{\partial \xi} + \eta_x\frac{\partial \tau_{xx}}{\partial \eta} + \eta_y\frac{\partial \tau_{yx}}{\partial \eta} + \eta_z\frac{\partial \tau_{zx}}{\partial \eta} + \zeta_x\frac{\partial \tau_{xx}}{\partial \zeta} + \zeta_y\frac{\partial \tau_{yx}}{\partial \zeta} + \zeta_z\frac{\partial \tau_{zx}}{\partial \zeta}\end{aligned} \tag{22}$$

$$\begin{aligned}\frac{\partial \rho v}{\partial t} &= v\left.\frac{\partial \rho}{\partial t}\right|_\xi + \rho\left.\frac{\partial v}{\partial t}\right|_\xi - \eta_x\frac{\partial \rho uv}{\partial \eta} - \eta_y\frac{\partial \rho vv+p}{\partial \eta} - \eta_z\frac{\partial \rho wv}{\partial \eta} - \zeta_x\frac{\partial \rho uv}{\partial \zeta} - \zeta_y\frac{\partial \rho vv+p}{\partial \zeta} - \zeta_z\frac{\partial \rho wv}{\partial \zeta} + \\ &+ \xi_x\frac{\partial \tau_{xy}}{\partial \xi} + \xi_y\frac{\partial \tau_{yy}}{\partial \xi} + \xi_z\frac{\partial \tau_{zy}}{\partial \xi} + \eta_x\frac{\partial \tau_{xy}}{\partial \eta} + \eta_y\frac{\partial \tau_{yy}}{\partial \eta} + \eta_z\frac{\partial \tau_{zy}}{\partial \eta} + \zeta_x\frac{\partial \tau_{xy}}{\partial \zeta} + \zeta_y\frac{\partial \tau_{yy}}{\partial \zeta} + \zeta_z\frac{\partial \tau_{zy}}{\partial \zeta}\end{aligned} \tag{23}$$

$$\begin{aligned}\frac{\partial \rho w}{\partial t} &= w\left.\frac{\partial \rho}{\partial t}\right|_\xi + \rho\left.\frac{\partial w}{\partial t}\right|_\xi - \eta_x\frac{\partial \rho uw}{\partial \eta} - \eta_y\frac{\partial \rho vw}{\partial \eta} - \eta_z\frac{\partial \rho ww+p}{\partial \eta} - \zeta_x\frac{\partial \rho uw}{\partial \zeta} - \zeta_y\frac{\partial \rho vw}{\partial \zeta} - \zeta_z\frac{\partial \rho ww+p}{\partial \zeta} + \\ &+ \xi_x\frac{\partial \tau_{xz}}{\partial \xi} + \xi_y\frac{\partial \tau_{yz}}{\partial \xi} + \xi_z\frac{\partial \tau_{zz}}{\partial \xi} + \eta_x\frac{\partial \tau_{xz}}{\partial \eta} + \eta_y\frac{\partial \tau_{yz}}{\partial \eta} + \eta_z\frac{\partial \tau_{zz}}{\partial \eta} + \zeta_x\frac{\partial \tau_{xz}}{\partial \zeta} + \zeta_y\frac{\partial \tau_{yz}}{\partial \zeta} + \zeta_z\frac{\partial \tau_{zz}}{\partial \zeta}\end{aligned} \tag{24}$$

$$\begin{aligned}\frac{\partial \rho e}{\partial t} &= \frac{1}{\gamma-1}\left.\frac{\partial p}{\partial t}\right|_\xi + \frac{u^2+v^2+w^2}{2}\left.\frac{\partial \rho}{\partial t}\right|_\xi + \rho u\left.\frac{\partial p}{\partial t}\right|_\xi + \rho v\left.\frac{\partial p}{\partial t}\right|_\xi + \rho w\left.\frac{\partial p}{\partial t}\right|_\xi - \\ &- \eta_x\frac{\partial u(\rho e+p)}{\partial \eta} - \eta_y\frac{\partial v(\rho e+p)}{\partial \eta} - \eta_z\frac{\partial w(\rho e+p)}{\partial \eta} - \zeta_x\frac{\partial u(\rho e+p)}{\partial \zeta} - \zeta_y\frac{\partial v(\rho e+p)}{\partial \zeta} - \zeta_z\frac{\partial w(\rho e+p)}{\partial \zeta} + \\ &+ \xi_x\frac{\partial \beta_x}{\partial \xi} + \xi_y\frac{\partial \beta_y}{\partial \xi} + \xi_z\frac{\partial \beta_z}{\partial \xi} + \eta_x\frac{\partial \beta_x}{\partial \eta} + \eta_y\frac{\partial \beta_y}{\partial \eta} + \eta_z\frac{\partial \beta_z}{\partial \eta} + \zeta_x\frac{\partial \beta_x}{\partial \zeta} + \zeta_y\frac{\partial \beta_y}{\partial \zeta} + \zeta_z\frac{\partial \beta_z}{\partial \zeta} \quad .\end{aligned} \tag{25}$$

Further details on the formulation of the boundary conditions may be found in reference [12].

The approximation for the lateral boundary conditions is obtained by assuming, that the shape of the boundaries is identical with streamline surfaces. Then, the kinematic flow condition can be implemented, for example at the top of the computational domain (plane $\overline{DCKL}$, Fig.1) the normal derivatives of the solution vector $\vec{Q}$ with respect to the slope of the local streamline vanish, if the flow is assumed to be inviscid. The pressure is determined by solving the momentum equation normal to the boundary, and the shock is fixed by prescribing the RANKINE-HUGONIOT relations at the bottom ($\overline{EF}$, Fig.1) of the computational domain.

Now let us make a few more remarks on the initial condition. As mentioned before a slender vortex is prescribed for the entire flow field and the shock is locally generated at the bottom of the computational domain at $t = 0$. The shock propagates into the interior of the flow field during the computation. In an

alternative approach the initial conditions are generated using a plane shock that divides the computational domain into two parts. Upstream of the shock again a slender vortex is prescribed whereas downstream of it a uniform flow is specified. The computations show that the initial conditions have barely any impact on the results obtained. Particularly in the case of breakdown, it can be clearly demonstrated that the flow inside the bubble is not affected by the varying initial conditions.

4. Computational Domain and Numerical Method

The computational domain is a rectangular box containing $99 \times 99 \times 199$ grid points in the x-y-, and z-direction (Fig. 1). Near the axis of the vortex the grid is clustered so that the vortex core ($-1 < r < 1$) is resolved with approximately 21 grid points in the radial $r = \sqrt{x^2 + y^2}$ direction.

The differentials in time and space are discretized to second order accuracy. The temporal integration is performed using a 5-step RUNGE-KUTTA scheme

$$\hat{Q}^{(n+1)} = \hat{Q}^n + \Delta t(\alpha_{m1} RHS(\hat{Q}^n) + \alpha_{m2} RHS(\ {}^1\hat{Q}) + \cdots + \alpha_{mm} RHS(\ {}^{m-1}\hat{Q})) \tag{25}$$

with the non-zero coefficients $\alpha_{11} = 0.059$, $\alpha_{22} = 0.145$, $\alpha_{33} = 0.273$, $\alpha_{44} = 0.500$ and $\alpha_{55} = 1.000$. Details of the optimization can be found in [17].

A node-centered scheme is used to approximate the inviscid and viscous fluxes. The convective fluxes are discretized using an explicit finite-volume scheme based on the $AUSM$ approach by LIOU & STEFFEN [7] and the $AUSM+$ approach by LIOU [8]. The EULER fluxes are written as a sum of the convective and pressure terms. The convective part is reformulated using the local speed of sound a, and the pressure is separately split on the cell interfaces. For example, the flux in the $x-$direction reads

$$\hat{E} = \underbrace{\begin{pmatrix} \rho u \\ \rho u u \\ \rho u v \\ \rho u w \\ \rho u (e + p/\rho) \end{pmatrix}}_{\hat{E}^K} + \underbrace{\begin{pmatrix} 0 \\ p \\ 0 \\ 0 \\ 0 \end{pmatrix}}_{\hat{E}^P} = \underbrace{\frac{U}{a}}_{\widetilde{Ma}} \underbrace{\begin{pmatrix} \rho a \\ \rho u a \\ \rho v a \\ \rho w a \\ \rho (e + p/\rho) a \end{pmatrix}}_{\mathcal{F}^K} + \underbrace{\begin{pmatrix} 0 \\ \widetilde{p}_+ + \widetilde{p}_- \\ 0 \\ 0 \\ 0 \end{pmatrix}}_{\hat{E}_a^P} \quad . \tag{26}$$

The convective part is represented by a MACH number weighted interpolation

$$\hat{E}_a^K = \frac{1}{2} \left[(\widetilde{Ma}_+ + \widetilde{Ma}_-) \left(\mathcal{F}_+^K + \mathcal{F}_-^K \right) + |\widetilde{Ma}_+ + \widetilde{Ma}_-| \left(\mathcal{F}_+^K - \mathcal{F}_-^K \right) \right] \quad . \tag{27}$$

The fluxes $\mathcal{F}_\pm^K$ are determined using variables interpolated via the $MUSCL$ approach from the left (+) and right (–) side of the interface, and the split MACH numbers ($\widetilde{Ma}_\pm$) are weighted by the interpolated MACH numbers ($\widehat{Ma}_\pm$) according to $\widetilde{Ma}_\pm = \frac{1}{2}\widehat{Ma}_\pm$. The split pressure $\widetilde{p}_\pm$ is given by $\widetilde{p}_\pm = \frac{1}{2} p_\pm$.

5. Results

The results for the oblique shock-vortex interaction for inviscid and viscous flows are presented first. Subsequently, the numerical results for the normal shock-vortex interaction are discussed, and some general remarks will be made concerning the interaction of slender vortices with both, oblique and normal shocks. Finally, a breakdown criterion is derived for the normal shock-vortex interaction.

Figures 2 and 3 show the color schlieren picture and some numerical data for the interaction of a slender BURGERS vortex and an oblique shock for free stream MACH numbers of $Ma_\infty = 1.6$ and $Ma_\infty = 2.0$. The solutions for the inviscid and the viscous flow and also the color schlieren picture confirm that the originally straight oblique shock is distorted into an 'S'-shaped shock front near the core of the vortex. The computations show that the deformation of the shock to an 'S'-shaped part depends on the shock angle, on the magnitude of axial component of the velocity on the vortex axis, and on the free stream MACH number. Since breakdown or the bursting of the vortex is necessarily connected with the formation of a stagnation point on or near the axis, it is necessary that the shock angle has to increase in the vicinity of the vortex core such that the flow downstream of the shock can be locally subsonic, and further, that the pressure rise across the deformed part of the shock is sufficient to initiate breakdown. The deformation of the shock is primarily influenced by the radial

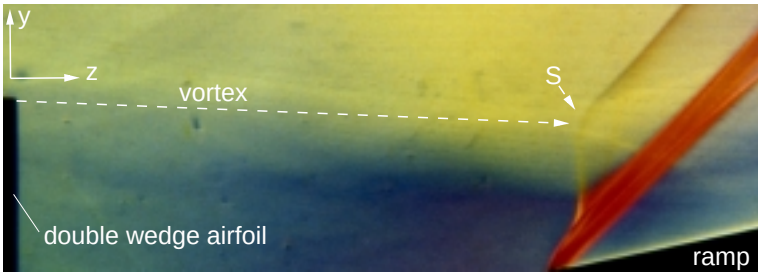

Fig. 2. Color schlieren picture of the oblique-shock vortex-interaction $Ma_\infty = 2.0$, Re=15000, (M. Klaas, private communications)

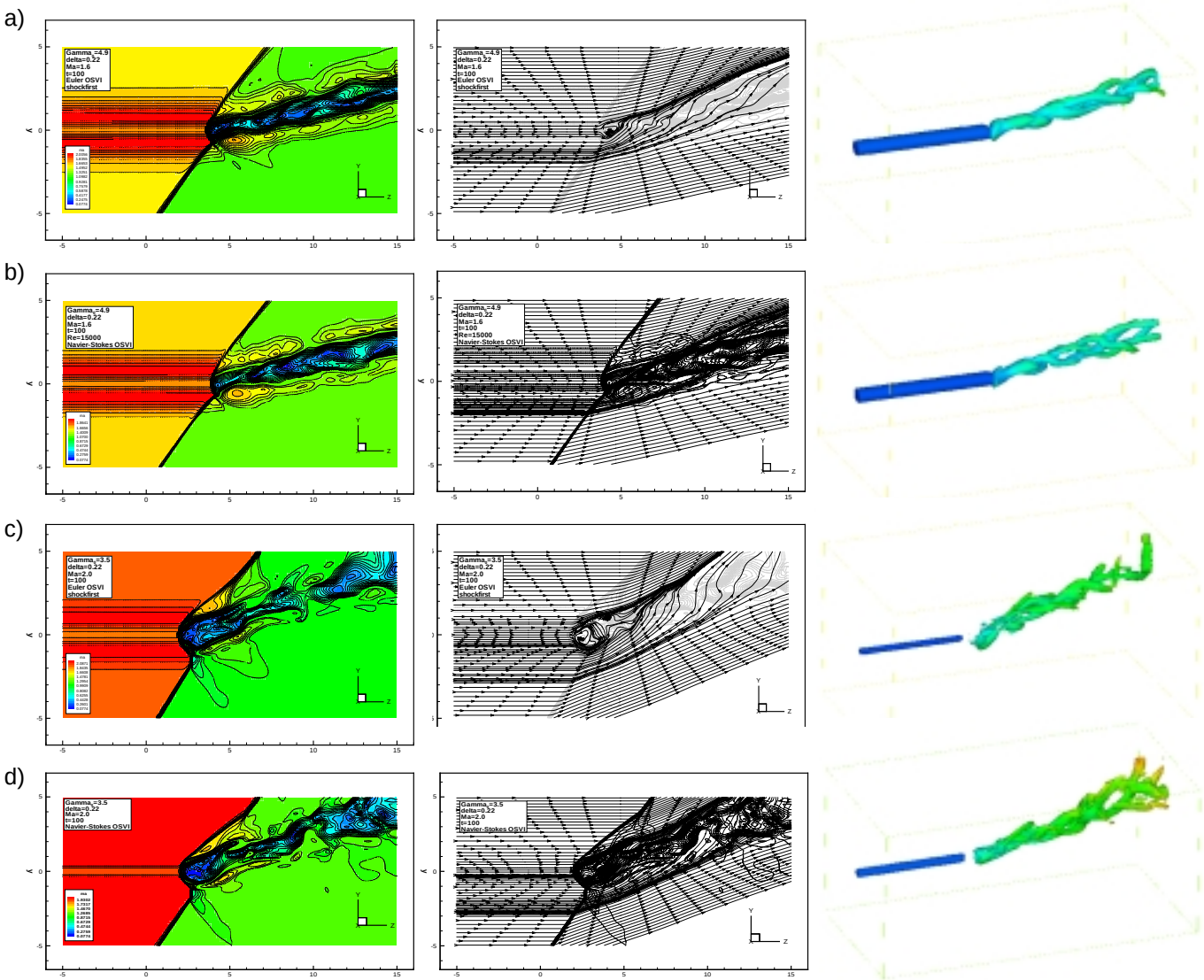

Fig. 3. MACH number distribution (1st column), streamlines (2nd column), and λ_2-iso surface (3rd column) for the oblique-shock vortex-interaction at time step $t = 200$. I) $Ma_\infty = 1.6$, $\Gamma_0 = 4.9$, $\delta = 0.22$, a) EULER computation, b) NAVIER-STOKES computation (Re=15000). II) $Ma_\infty = 2.0$, $\Gamma_0 = 3.5$, $\delta = 0.22$, a) EULER computation , b) NAVIER-STOKES computation (Re=15000). Flow is in the positive z-direction.

distribution of the axial velocity component, and the pressure jump across the shock is mainly dictated by the free stream MACH number and the wedge angle, that generates the shock.

Figure 3 evidences a recirculation region inside the burst part of the vortex. It is moved upward away from the axis of the undisturbed vortex. The distribution of the λ_2 contours (3rd column, Fig. 3) indicates divided vortex tubes downstream from the burst part of the vortex, indicating the change to spiral type breakdown.

Normal shock vortex breakdown differs from that caused by oblique shocks. If the so-called bubble-type breakdown occurs, the flow inside the burst part of the vortex is generally characterized by the formation of a stagnation point on the vortex axis, followed by a reversed flow region further downstream. Either a small axial or large azimuthal velocity component can trigger breakdown. The larger the pressure rise or the circulation the more likely breakdown will occur. The breakdown is more probable in interactions with normal than with oblique shocks. Since the subsonic flow downstream from a normal shock differs from that downstream from an oblique shock, the structure of the burst part of the vortex is also different. In the case of normal shock-vortex interaction the shock migrates upstream in the course of time, yielding a cone-like shock shape. Depending on the free stream MACH number, the circulation, and the radial profile of the axial velocity component two types of flow fields can emerge.

Figure 4 shows a sequence of instantaneous pictures of the interaction between a vortex of circulation Γ=2.5, (δ=0.1) and a normal shock at a free stream MACH number of Ma_∞=1.6 for various times $t = t^*/(l_0^* a_0^*) =$ 60..200. The numerical results show a small region of reversed flow with two free stagnation points on the axis at the beginning of the breakdown process. The first stagnation point is formed at a certain distance downstream from the shock and the second stagnation point terminates the region of reversed flow (Fig. 4, 4th column, t=100) inside the bubble. With increasing time the stagnation point is shifted in the z-direction. The reverse flow causes the shock to move upstream, and a bubble-like flow structure emerges, growing in the axial and radial direction until the upstream stagnation point reaches a stable position. Further downstream from the shock, which remains normal near the axis of the vortex but is curved further away from it, the flow is unsteady, slightly oscillating.

The dependence of the onset of vortex bursting on the characteristic flow parameters was clearly evidenced in the calculations. For example, the results show that a reduction of the axial velocity or an increase of the azimuthal velocity component enhance breakdown. In other words, the stronger the shock and hence the pressure jump, the less the circulation has to be to cause breakdown, and for weaker shocks a larger circulation is necessary for breakdown.

Another observation was made by changing the radial, originally uniform profile of the axial velocity component into a wake-like profile. Breakdown would then occur earlier, since the necessary deceleration of the axial flow to reach a stagnation point is smaller than for a uniform or even a jet-like profile. These results agree with the criterion derived in [2] for incompressible flows. It predicts breakdown, when the ratio of the maximum azimuthal and the axial velocity components reaches a certain value.

The reversed flow inside the vortex bubble can be explained using several small identifiable ring-like vortex structures (Fig. 4, 3th column) traveling downstream with progressing time. The velocity and MACH number distributions evidence a strong axial reverse flow along the axis of the vortex, and the ring-like vortex structures inside the bubble are confirmed visualizing the vorticity contours. With increasing time the flow deviates more and more from its initial axial symmetry. Hence, it can be concluded that vortex breakdown is a truly three-dimensional process which cannot be described with a formulation for axially symmetric flows.

We turn now to the discussion of the differences between inviscid and viscous flow computations. Figure 5 shows the burst part of the vortex for normal-shock interaction at Ma_∞=1.6, Γ_0=5.0, for time level t=200 for the inviscid (left column) and the viscous flow computation (Re=15000, right column). In the upper pictures the three-dimensional vorticity distribution is exhibited. In these figures the MACH number distribution of the x-z symmetry plane is also projected onto the boundary surface of the computational domain. It can be seen that the inviscid flow computation (left column) yields larger vortical structures than the viscous flow computation. The MACH number contours exhibit a multiple shock structure. The deformed shock resembles that of a bow shock observed at supersonic flow around blunt bodies. Further away from the axis the shock angle decreases until a triple point is encountered. The calculation for inviscid flow yields two adjacent clockwise rotating vortex rings inside the bubble, while for the viscous flow computations multiple vortex structures can be observed. An analysis of the time-development of the flow shows a periodic generation and shedding of the vortex rings. A detailed investigation of the inviscid flow pattern evidences that the two vortices are separated by a shock which is caused by a supersonic jet-like flow in the upstream direction along the axis (Fig. 5). This shock is perpendicular to the z-axis. The streamlines in the recirculation region show a convergent-divergent nozzle-like flow structure that enables the upstream flow to become supersonic inside the bubble. Such an acceleration to supersonic flow was already noticed by ERLEBACHER ET AL. in their numerical investigations [4].

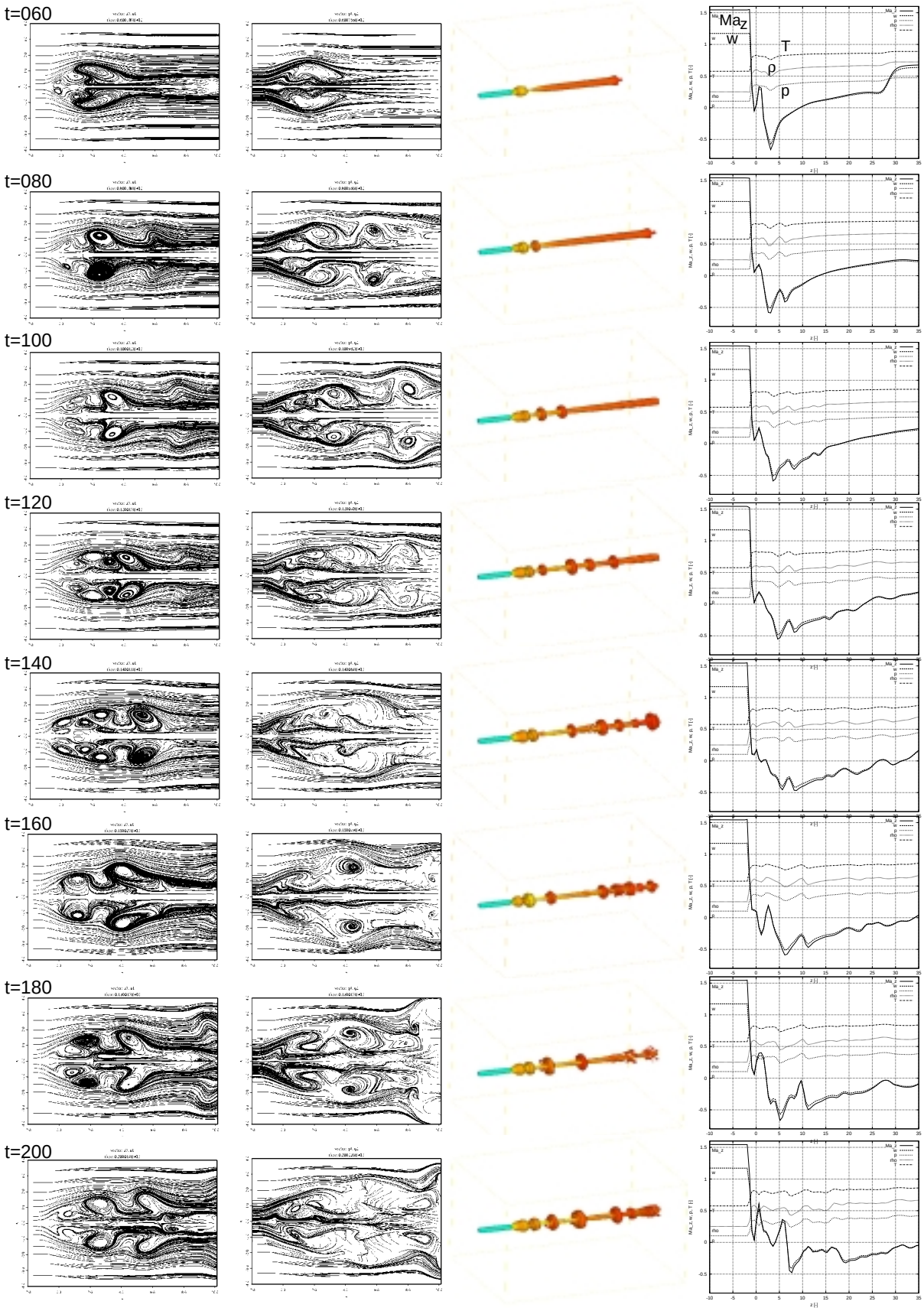

Fig. 4. Temporal evolution of streamlines (1st column), and vortex lines (2nd column) in the center plane $y = 0$; λ_2-iso surface (3rd column); primitive variables and MACH number (4th column) for certain time steps in the case of normal shock-vortex interaction ($Ma_\infty = 1.6$, $\Gamma_0 = 2.5$, $\delta = 0.1$, Re=15000).

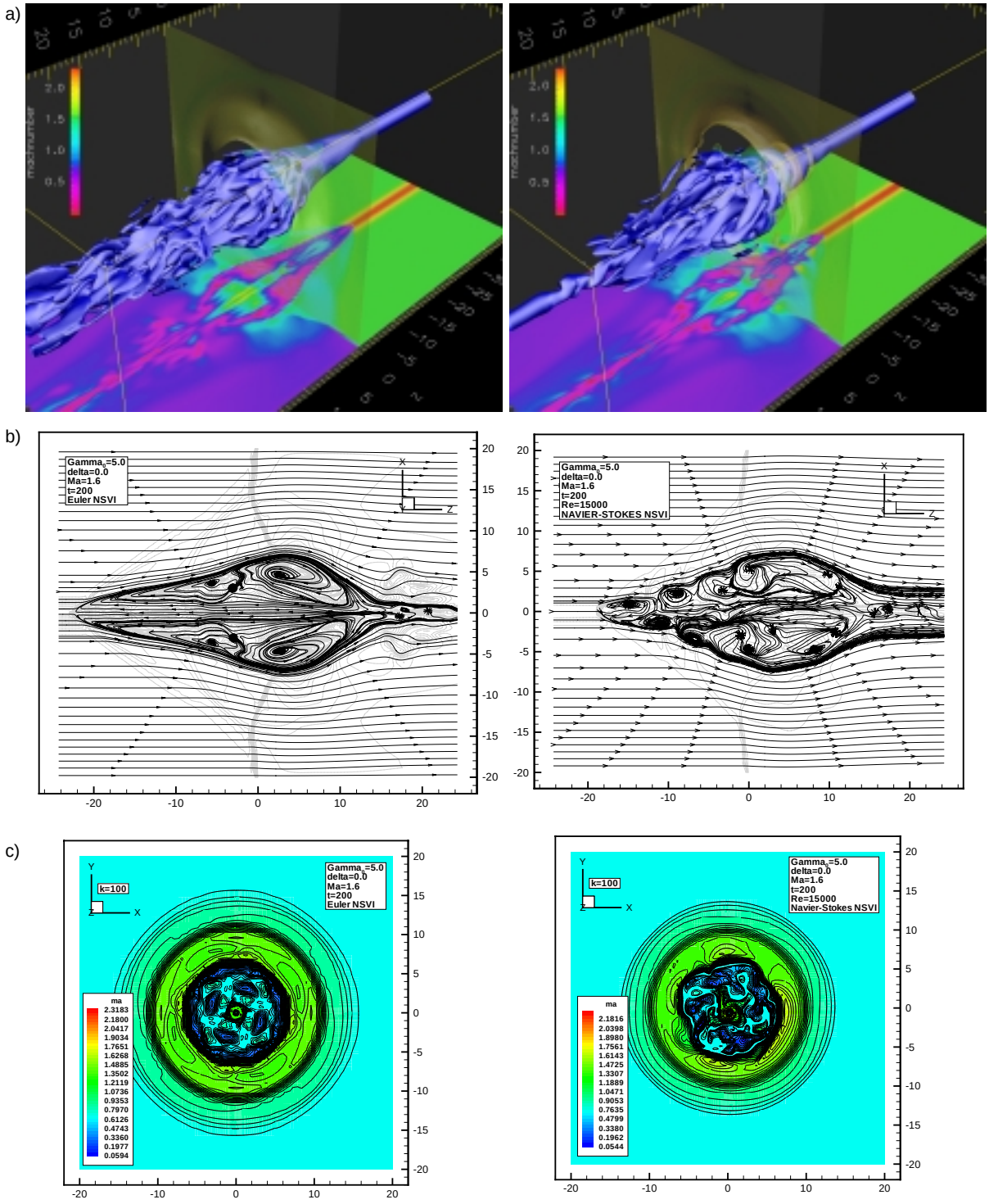

Fig. 5. Instantaneous pictures at time step t=200 of the EULER (left column) and NAVIER-STOKES (right column) computations (Ma_∞=1.6, Γ_0=5.0, δ=0, and Re=15000). a) Spatial iso-vorticity surface combined with the MACH number distribution mapped into the surface plane, b) streamline patterns in the x-z-plane at y=0 of the bubble, and c) MACH number distribution in a cross section of the bubble slice at the x-y-plane for $z = 0$.

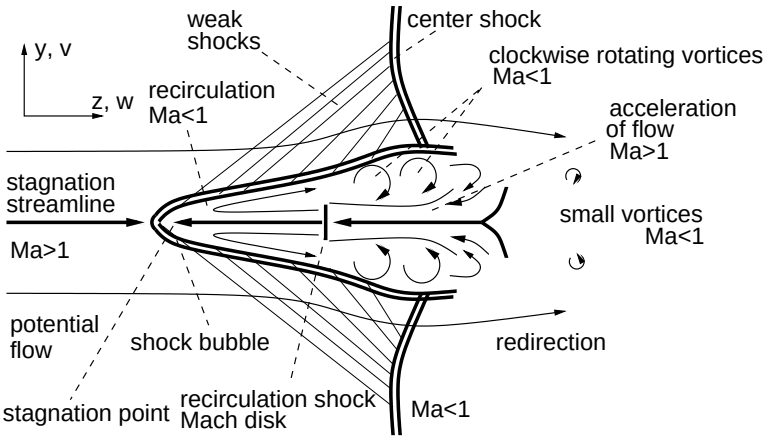

Fig. 6. Flow schematic for strong vortex breakdown.

In the lower part of figure 5 the MACH number distribution in a plane perpendicular to the vortex axis is shown. A fan like flow regime with multiple shock structures can be observed which also was noticed by BRILLANT ET AL. in their experiments [2]. To clarify the details of the flow in the x-z-plane a schematic diagram of the flow in the bubble is given in figure 6.

Fig. 7 shows a comparison of a schlieren picture with the bubble topology of the computation. In the experimental investigations the vortex is produced using a double wedge airfoil in a supersonic flow. When vortex breakdown occurs, the shock is deformed and moves upstream, and the characteristic length scale of the arising bubble is of the order of the diameter of the core of the impinging vortex. Both investigations yield qualitatively the same result.

In addition to the numerical and experimental investigations a breakdown criterion is derived for uniform axial flow (Fig. 8). Based on the axial momentum equation for inviscid flow and the RANKINE-HUGONIOT relations, the onset of breakdown can be predicted by requiring a stagnation point to be formed on the axis. In [14] such a condition is formulated along the vortex axis

$$\underbrace{\frac{p^*_{1_{AXIS}}}{p^*_{1_\infty}}}_{I} + \underbrace{\frac{\rho^*_{1_{AXIS}} \cdot v^{2*}_{z1_{AXIS}}}{p^*_{1_\infty}}}_{II} \geq \underbrace{\frac{p^*_{2_\infty}}{p^*_{1_\infty}}}_{III} \quad . \tag{28}$$

In the above equation the pressure and momentum forces are related to the free stream pressure $p^*_{1_\infty}$. In the case of uniform axial flow the second term (II) on the left hand side can be cast into the following form

$$\frac{\rho^*_{1_{AXIS}} \cdot v^{2*}_{z1_{AXIS}}}{p^*_{1_\infty}} = \gamma \cdot \frac{\rho^*_{1_{AXIS}}}{\rho^*_{1_\infty}} \cdot Ma^2_{1_\infty} \quad . \tag{29}$$

Since CROCCO+S vorticity relation yields $T\nabla s = \nabla h_0$ if the velocity and the vorticity vector are parallel to each other in steady flows the radial momentum equation for slender vortices $\frac{\partial p^*}{\partial r^*} = \frac{\rho^* v^{2*}_\varphi}{r^*}$ can be solved for the velocity distribution given by equation (8). Together with the RANKINE HUGONIOT relation for the pressure ratio across a normal shock (term III) $p^*_2/p^*_1 = 1 + \frac{2\cdot\gamma}{\gamma+1}(Ma^2_\infty - 1)$, the axial momentum equation (29) leads to the following breakdown criterion

$$\underbrace{\left(1 - \frac{(\gamma-1)\cdot\Gamma_0^2\cdot e^1}{16\pi^2[2+(\gamma-1)Ma^2_\infty]^{-1}}\right)^{\frac{\gamma}{\gamma-1}}}_{p^*_{1_{AXIS}}/p^*_{1_\infty}} + \underbrace{\frac{\gamma Ma^2_{1_\infty}}{\left(1 - \frac{(\gamma-1)\Gamma_0^2\cdot e^1}{16\pi^2[2+(\gamma-1)Ma^2_\infty]^{-1}}\right)^{\frac{-1}{\gamma-1}}}}_{\rho^*_{1_{AXIS}}/\rho^*_{1_\infty}} \geq \underbrace{1 + \frac{2\gamma}{\gamma+1}(Ma^2_\infty - 1)}_{p^*_{2_\infty}/p^*_{1_\infty}} \quad . \tag{30}$$

From the above equation the circulation Γ_0 for which breakdown occurs can be determined as a function of Ma_∞. Using equation (12) that connects the spiral angle τ and the circulation Γ_0 we arrive at an expression for τ depending on Ma_∞. The comparison of the results obtained with the relation $\tau = \tau(Ma_\infty)$ and with numerical and experimental data [3, 4, 9] shows good agreement in the range of $1.5 \leq Ma_\infty \leq 2.0$ (Fig. 8).

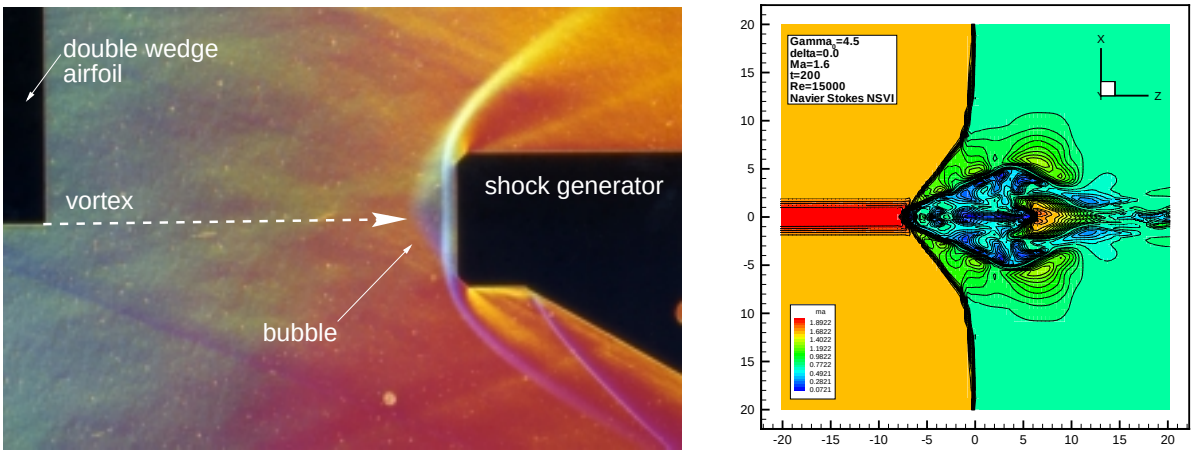

Fig. 7. Color schlieren picture (M. Klaas, private communications) (left) and numerical MACH number distribution (right) at $Ma_\infty = 1.6$, Γ_0=4.5, δ=0 for uniform axial flow at Re=15000. Flow is from left to right.

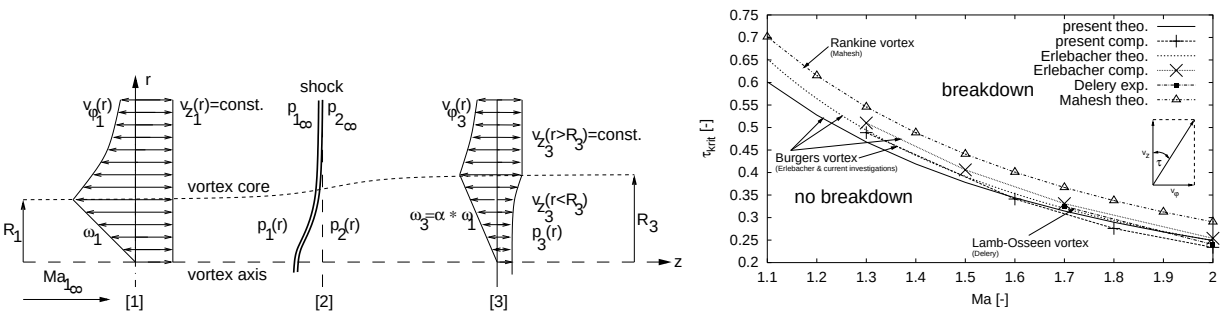

Fig. 8. Theoretical model to predict vortex breakdown (left) and breakdown map for normal shock vortex interaction (right).

5.1. Conclusions

Breakdown of slender vortices in supersonic flow caused by the interaction with normal and oblique shocks was investigated using numerical solutions of the EULER and NAVIER-STOKES equations. The calculations show, that a normal shock interacting with a slender vortex does not necessarily lead to breakdown. If the circulation of the vortex is small and if the axial velocity profile is uniform, the vortex does not change its overall shape. By increasing the vortex strength, the free stream MACH number and a wake-like axial flow profile, a free stagnation point on or near the axis of the vortex can be formed. This can be considered as the initiation of vortex breakdown. The results obtained indicate that the flow structure of the burst part of the vortex as simulated with the numerical solution agrees well with experimental observations. Several ring-like, slightly oscillating vortex structures are formed immediately downstream from a stagnation point on the axis. For certain flow conditions strong upstream flow motion, even supersonic flow may occur near the axis. A breakdown criterion was derived that shows good agreement with the numerical and experimental findings and other data from the literature.

Acknowledgments

Grateful acknowledgment is due to the Deutsche Forschungsgemeinschaft for supporting this research. Mr. M. Klaas (Aerodynamisches Institut, RWTH-Aachen) provided the color schlieren pictures.

Addresses: Dipl.-Ing. O. Thomer, Prof. Dr. -Ing. W. Schröder, and Prof. em. E. Krause, Ph.D., Aerodynamisches Institut, RWTH Aachen, Wüllnerstr. zw. 5 u. 7, 52062 Aachen, Germany.

References

[1] Althaus W., Weimer M. Review of the Aachen Work on Vortex Breakdown. IUTAM Symposium on Dynamics of Slender Vortices, E. Krause and K. Gersten (Ed.), Kluwer Academic Publishers, 1997. P. 331–344.

[2] Billant P., Chomaz J. M., Delbende I., Huerre P., Loiseleux T., Olendraru C., Rossi M., Sellier A. Instabilities and Vortex Breakdown in Swirling Jets and Wakes. IUTAM Symposium on Dynamics of Slender Vortices, (Eds. E. Krause, K. Gersten), Kluwer Academic Publishers, 1997. P. 267–286.

[3] Delery J. Aspects of Vortex Breakdown, Prog. Aerospace Sci. 1994. Vol. 30, P. 1–59.

[4] Erlebacher G., Hussaini M., Shu C. Interaction of a Shock with a Longitudinal Vortex. ICASE Report, No. 96–31, 1996.

[5] Kandil O., Kandil H., Liu C. Computation of Steady and Unsteady Compressible Quasi-Axisymmetric Vortex Flow and Breakdown // AIAA Paper 91–0752, 1991.

[6] Kandil O., Kandil H., Liu C. Shock/Vortex Interaction and Vortex-Breakdown Modes. IUTAM Symposium of Fluid Dynamics of High Angle of Attack, Tokyo, Schumann et al. (Ed.), Springer Verlag, 1992.

[7] Liou M., Steffen C. A New Flux Splitting Scheme // J. of Comput. Phys. 1993. Vol. 107. P. 23–39.

[8] Liou M. A Sequel to AUSM: AUSM$^+$ // J. of Comput. Phys. 1996. Vol. 129. P. 364–382.

[9] Mahesh K. A Model for the Onset of Breakdown in an Axisymmetric Compressible Vortex // Physics of Fluids. 1996. Vol. 8, no. 12, P. 3338-3345.

[10] Menne S. Rotationssymmetrische Wirbel in achsparaller Strömung. PhD Thesis, Aerodynamisches Institut, RWTH Aachen, 1986.

[11] Poinsot T. J., Lele S. K. Boundary Conditions for Direct Simulations of Compressible Viscous Flows // J. of Comput. Phys. 1992. Vol. 101. P. 104–129

[12] Rister T. Grobstruktursimulation schwach kompressibler turbulenter Freistrahlen - ein Vergleich zweier Lösungsansätze. PhD Thesis, Aerodynamisches Institut, RWTH Aachen, 1998.

[13] Schlechtriem S., Lötzerich M. Breakdown of tip leakage vortices in compressors at flow conditions close to stall. IGTI-ASME conference, Orlando Florida, June 1997.

[14] Thomer O., Krause E., Schröder W., Meinke M. Computational Study of Normal and Oblique Shock-Vortex Interactions. European Congress on Computational Methods in Applied Sciences and Engineering, ECCOMAS 2000, Barcelona 11–14. September, 2000.

[15] Thompson K. Time Dependent Boundary Conditions for Hyperbolic Systems // J. of Comput. Phys. 1987. Vol. 68, No. 1. P. 1–24.

[16] Thompson K. Time Dependent Boundary Conditions for Hyperbolic Systems II // J. of Comput. Phys. Vol. 89. P. 439–461, 1990.

[17] Yu S. Runge-Kutta Methods Combined with Compact Difference Schemes for the Unsteady Euler Equations. NASA Technical Memorandum 105834, ICOMP–92–12, CMOTT–92–08. 1992. P. 127–161.